



# Air-sea interactions in the marginal ice zone

Seth Zippel<sup>1\*</sup> • Jim Thomson<sup>1</sup>

<sup>1</sup>Applied Physics Laboratory, University of Washington, Seattle, Washington, United States

\*zippelsf@apl.washington.edu

---

## Abstract

The importance of waves in the Arctic Ocean has increased with the significant retreat of the seasonal sea-ice extent. Here, we use wind, wave, turbulence, and ice measurements to evaluate the response of the ocean surface to a given wind stress within the marginal ice zone, with a focus on the local wind input to waves and subsequent ocean surface turbulence. Observations are from the Beaufort Sea in the summer and early fall of 2014, with fractional ice cover of up to 50%. Observations showed strong damping and scattering of short waves, which, in turn, decreased the wind energy input to waves. Near-surface turbulent dissipation rates were also greatly reduced in partial ice cover. The reductions in waves and turbulence were balanced, suggesting that a wind-wave equilibrium is maintained in the marginal ice zone, though at levels much less than in open water. These results suggest that air-sea interactions are suppressed in the marginal ice zone relative to open ocean conditions at a given wind forcing, and this suppression may act as a feedback mechanism in expanding a persistent marginal ice zone throughout the Arctic.

---

## Introduction

Waves are becoming increasingly important in the Arctic Ocean, which has experienced a significant retreat of the seasonal ice extent (Comiso and Nishio, 2008; Comiso et al., 2008). Thomson and Rogers (2014) showed that the increased fetch in the Beaufort and Chukchi Seas is associated with large wave heights, far beyond what had previously been observed. Their work extends measurements from satellite data (Francis et al., 2011) and model hindcasts (Wang et al., 2015) which have shown a statistically significant increase in mean wave heights for this region over the past decades. Increased wave heights are of particular significance as Kohout et al. (2014) recently found that the attenuation rate of large waves in ice is linear, as opposed to the exponential decay typically assumed. Thus, as wave energy increases throughout the Arctic, waves are likely to propagate farther into the ice.

Increased wave energy in the Arctic ice pack has implications beyond accelerated ice break-up. Waves have been shown to increase the exchange of momentum, heat and gasses between ocean and atmosphere, as recently reviewed by D'Asaro et al. (2014). The pathway of wave energy into ocean mixing is less clear, but is often attributed to wave breaking very near the surface (Agrawal et al., 1992; Craig and Banner, 1994; Terray et al., 1996) and to Langmuir turbulence lower in the surface layer (as reviewed by Thorpe, 2004). Turbulence has particular importance for gas transfer, where the turbulent kinetic energy (TKE) dissipation rate at the ocean surface is commonly used to estimate gas transfer velocity (as originally proposed by Lamont and Scott, 1970, and more recently employed by Zappa et al., 2003, and Loose et al., 2014). In addition to mixing, waves provide the roughness which determines drag (Chalikov and Belevich, 1993), and thus sea state modifies air-sea momentum exchange. Exchanges of momentum, heat, and gasses are of particular importance in regions of partial ice cover, as the Arctic may be in transition from an ocean driven by thermohaline processes to one driven by atmospheric forcing (Rainville et al., 2011).

## Domain Editor-in-Chief

Jody W. Deming, University of Washington

## Associate Editor

Eddy C. Carmack, Fisheries & Oceans Canada

## Knowledge Domain

Ocean Science

## Article Type

Research Article

## Part of an *Elementa* Special Feature

Marginal ice zone processes in the summertime Arctic

Received: July 31, 2015

Accepted: February 14, 2016

Published: March 31, 2016

Sparse measurements of waves in ice make parameterization of air-sea interactions in partial ice cover difficult, and therefore models of air-sea interaction often use open water parameterizations for waves (e.g., for air-ocean drag in Martin et al., 2014). However, waves in ice are both damped and scattered (Wadhams et al., 1986, 1988; Squire, 2007). Therefore, it is likely that changes in the wave field alter air-sea exchanges in partial ice cover, such that they may be dramatically different from open water values.

## Radiative transfer equation

The radiative transfer equation describes the evolution of wave energy per unit frequency,  $E(f)$ , as balanced by source and sink terms:

$$\frac{dE(f)}{dt} + \mathbf{c}_g \cdot \nabla E(f) = S_{wind} - S_{dis} + S_{nl} - S_{ice}. \quad (1)$$

Here,  $f$  is the intrinsic wave frequency,  $\nabla$  is the horizontal derivative operator,  $\mathbf{c}_g$  is the wave group velocity,  $S_{wind}$  is the wind input term,  $S_{dis}$  is the wave dissipation term, often associated with wave breaking,  $S_{nl}$  describes energy transfers between frequencies, and  $S_{ice}$  governs wave-ice interaction. The wave-ice interactions can be both conservative (i.e., scattering) and non-conservative (i.e., damping). Typically, the energy spectrum,  $E(f)$  and source/sink terms,  $S$ , are functions of both frequency and direction  $E(f, \theta)$ ,  $S(f, \theta)$ . For this study we used the one dimensional variance spectrum  $E(f)$ , and source/sink terms  $S(f)$ .

Of these sources and sinks,  $S_{wind}$  can be measured directly, and is dependent on the wave action density, radian frequency  $\omega = 2\pi f$ , and a dimensionless parameter  $\beta$  (Tolman and Chalikov, 1996),

$$S_{wind} = \beta \omega E(f). \quad (2)$$

$\beta$  can be estimated from co-temporal measurements of pressure and wave height (Plant, 1982), and has been shown to be dependent on the wave phase speed,  $c$ , the difference in direction of the wind and the waves,  $\theta_r$ , and the wind stress, either through  $u^*$  or a wind speed and drag coefficient. Plant (1982) parameterized  $\beta$  as:

$$\beta = (0.04 \pm 0.02) \left(\frac{u^*}{c}\right)^2 \cos(\theta_r). \quad (3)$$

Hence, the wind input term,  $S_{wind}$ , can be estimated with wave spectral measurements and directional wind stress measurements.

Terray et al. (1996) estimated the total mechanical energy flux from the wind to the waves by integrating the wind source term in frequency,

$$F = \rho g \int S_{wind} d\omega = \rho g \int \beta \omega E(\omega) d\omega, \quad (4)$$

(where  $\rho$  = density and  $g$  = gravitational acceleration) and then assumed that this flux into the waves was equal to the TKE flux from the waves into the ocean surface. This is a local balance, similar to the equilibrium defined by Phillips (1985). Terray et al. (1996) successfully used flux,  $F$ , and the significant wave height,  $H_s$ , in open water to normalize the depth-dependent turbulent dissipation rate,  $\epsilon(z)$  below the surface. In the absence of full wave spectral measurements, the energy flux into the wave field can be approximated as the wind stress multiplied by an effective transfer velocity,  $F = \tau c_{eff}$  (Gemrich et al., 1994). Subsequently, Terray et al. (1996) showed  $c_{eff}$  to be a function of wave age. In effect, the transfer velocity is a bulk representation of the wave spectral information and momentum transfer function, as included in Equation 4.

The ice source/sink,  $S_{ice}$ , primarily governs the decay of wave energy with distance from the sea-ice edge (Squire, 2007, and references therein). These decay rates are typically exponential for waves less than 3m (Wadhams et al., 1986; Kohout et al., 2014), occurring over scales longer than the scales of wave lengths (i.e., decays over tens to hundreds of kilometers, compared with wavelengths that are typically tens to hundreds of meters). Thus, the wave energy damping in  $S_{ice}$  is set mostly by non-local parameters: the open water wave energy levels, the horizontal distance from the ice edge, and the ice properties.

In contrast, the more localized wind source term,  $S_{wind}$ , is the focus of this paper. Observations of winds, waves, and ocean turbulence in the marginal ice zone are presented with a focus on local wind input to waves and subsequent ocean surface turbulence. Description of the methods and instrument deployments is followed by presentation and discussion of the bulk measurements, wave spectra, spectral directions, and turbulent dissipation rate profiles, including a rough estimate of the air-ocean drag coefficient in partial ice cover.

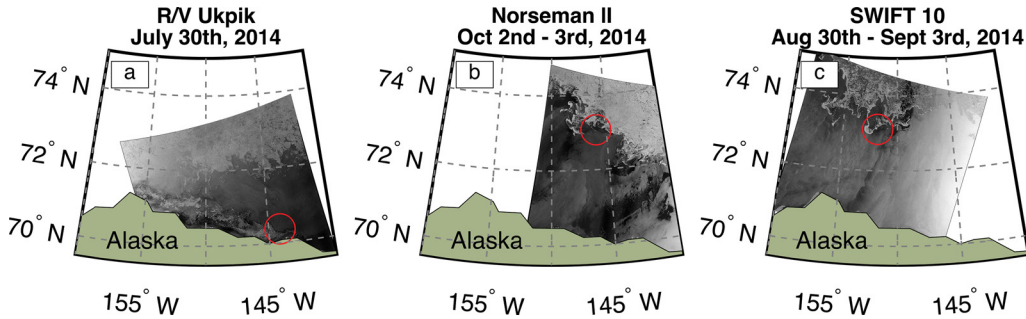


**Figure 1**  
Deployment locations.

Data were collected on two cruises in the summer of 2014: from the R/V *Ukpik* in July (a), and from the *Norseman II* in September/October (b). Unaccompanied buoys deployed from the *Ukpik* encountered ice on August 31st (c). Red circles overlaid on Radarsat-2 SAR images taken within 1 day of deployments show approximate locations of measurements relative to ice. SAR from NIC, processed by CSTARS and curated by Luc Rainville.

doi: 10.12952/journal.elementa.000095.f001

## Methods

### *Cruises and deployments*

Data were collected from two research cruises, on the R/V *Ukpik* (July 25th to August 2nd, 2014) in and out of Prudhoe Bay, AK, and on the *Norseman II* (September 26th–October 3rd) from Wainwright to Prudhoe Bay, AK. Shipboard observations included wind measurements and video recordings of sea ice. In addition, buoy observations of wave spectra and TKE dissipation rate were collected on July 30th from the R/V *Ukpik* (Figure 1a), and on October 2nd and 3rd from the *Norseman II* (Figure 1b). Two buoys were left to drift between the cruises, but do not have co-located shipboard measurements of wind stress and ice. One of the unaccompanied drifting buoys encountered ice on August 31st, 2014 (Figure 1c).

On July 30th, a Datawell Waverider buoy was deployed in open water, while a SWIFT buoy was progressively moved to areas of larger ice coverage within 1 km of the open water buoy. On October 2nd, one SWIFT buoy was deployed in ice-free water, while a second SWIFT buoy was deployed in 1% ice, eventually free drifting into 50% brash ice. The average distance between buoys on October 2nd was less than 1 km, with a maximum distance roughly 1.5 km. Of the two unaccompanied buoys, only one encountered ice, while the other stayed in open water at a range of roughly 20 km. The deployments described above, therefore, have co-temporal in-ice and ice-free wave measurements, along ice-perpendicular lines. The October 2nd deployment only has co-located ship-based measurements (wind stress and ice fraction) with the buoy in the ice for the first and last sampling period of the deployment, because the ship moved away to continue other sampling between deployment and recovery.

Finally, a similar deployment of several hours was conducted on October 3rd, 2014. However, a freezing event took place, such that the fractional ice coverage became difficult to define, with nearly 100% of the water surface covered with grease/shuga ice while small waves were present.

### *Wind stress*

Wind speeds were measured from a shipboard sonic anemometer sampling at 10 Hz. Wind stress was estimated using the inertial method of Large and Pond (1981), as described by Yelland et al. (1994). Wind data were processed in 10-minute intervals. Wind directions originating from the ship's stern were often contaminated by the ship's bridge, and were excluded from analysis. The velocity time series were despiked using the phase-space method of Goring and Nikora (2002), as implemented by Mori et al. (2007), with cubic interpolation replacement. Wind velocity spectra for the horizontal components  $E_{wind,uu}$  and  $E_{wind,vv}$  were estimated using the Welch method, where 512 point windows were de-trended, tapered with a Hamming window, and averaged with 75% overlap giving approximately 20 degrees of freedom. Frequencies between 1 and 4 Hz were confirmed to have an  $f^{-5/3}$  dependence, consistent with an inertial subrange. Mean correlations with  $f^{-5/3}$  spectral slopes in the inertial subrange were  $R^2 = 0.85$ , and all the spectra used were correlated at least  $R^2 > 0.7$ .

The ensemble spectra were fit to  $f^{-5/3}$ , and the air-side dissipation was estimated assuming advection of a frozen field (Taylor's hypothesis) at a speed  $U$ , such that

$$u_* = \left( \kappa \left( \frac{\langle E_{wind}(f) f^{5/3} \rangle}{K \left( \frac{U}{2\pi} \right)^{2/3}} \right)^{3/2} z_{wind} \right)^{1/3}, \quad (5)$$

where here,  $\langle \rangle$  represents an average from  $f = 1$  to 4 Hz,  $K = 0.55$  is the horizontal Kolmogorov constant,  $\kappa = 0.4$  is the von Karman constant and  $z_{wind}$  is the measurement height above the still water level (10.3 m for the *Norseman II*, 4.5 m for the R/V *Ukpik*). This representation assumes neutral stability, which is justified by the similarity of water, air, and sea-ice temperatures during the observations (typically within 5° C).

The unaccompanied buoy did not have co-located measurements from a sonic anemometer. Therefore, a drag coefficient of  $C_d = 1.5 \times 10^{-3}$  is assumed, and the friction velocity is found with  $u_* = C_d^{1/2} U_{10}$ .

### Wave spectra

Wave spectra were measured from surface tracking SWIFT buoys (Thomson, 2012). Velocity and acceleration data from a 9-axis IMU (Microstrain 3DM-GX3-35) collected at 4 Hz were used to make wave spectra. The horizontal velocity and vertical acceleration time series were filtered with a high-pass RC filter in the time domain. Horizontal velocity spectra were found using the Welch method, where the time series is split into 256 second windows with 75% overlap; a Hamming taper was applied to each window, and then the windows were averaged together, giving each 10-minute spectrum approximately 28 degrees of freedom. Wave energy spectra were estimated using linear theory, which relates horizontal wave orbital velocities to surface elevation, a method developed by Herbers et al. (2012):

$$E(f) = \frac{E_{UU}(f) + E_{VV}(f)}{(2\pi f)^2}, \quad (6)$$

where  $E(f)$  is the wave energy spectrum in  $\text{m}^2 \text{Hz}^{-1}$ ,  $E_{UU}(f)$  and  $E_{VV}(f)$  are the horizontal velocity spectra, and  $f$  is intrinsic wave frequency.

The acceleration spectra were used as a quality control for the wave orbital shapes, and to estimate the wave directional moments. As described in Herbers et al. (2012), the directional moments are found from,

$$\begin{bmatrix} a_1 \\ b_1 \end{bmatrix} = \begin{bmatrix} Q_{xz} / \sqrt{E_{zz}(E_{xx} + E_{yy})} \\ Q_{yz} / \sqrt{E_{zz}(E_{xx} + E_{yy})} \end{bmatrix}, \quad (7)$$

where  $Q_{xz}$  and  $Q_{yz}$  are the quadrature-spectra of horizontal and vertical displacements. The wave direction and directional spread are then found from the directional moments,

$$\theta(f) = \arctan(b_1/a_1), \quad (8)$$

and

$$\sigma_\theta(f) = \sqrt{2 \left( 1 - \sqrt{a_1^2 + b_1^2} \right)}. \quad (9)$$

### Turbulence

Turbulent dissipation rates in the upper half meter of the ocean were estimated using the second order structure function of velocities recorded from a Nortek 2 MHz Aquadopp HR mounted underneath the SWIFT drifters (Thomson, 2012). Velocities,  $u(z)$ , recorded at 4 Hz, in 4-cm bins were processed in 10-minute bursts. The structure function, defined as,

$$SF(z) = \langle [u(z) - u(z+r)]^2 \rangle, \quad (10)$$

is related to turbulent dissipation through,

$$SF = C_v^2 \epsilon^{2/3} r^{2/3}, \quad (11)$$

where here,  $\langle \rangle$  represents a time average,  $C_v^{-2} \approx 2.1$  is a constant,  $\epsilon$  is the turbulent dissipation rate, and  $r$  is the separation distance between measurements (Wiles et al., 2006). Dissipation rates are found by fitting the structure function to a  $r^{2/3}$  dependence, such that  $SF(z) = B(z)r^{2/3} + N$ , where  $N$  is the expected doppler noise offset. The slope coefficients,  $B(z)$ , can be used to estimate the turbulent dissipation rate by

$$\epsilon(z) = C_v^{-3} B(z)^{3/2}. \quad (12)$$

The Aquadopp was mounted such that beam #1 was oriented 60 degrees counterclockwise from the buoy's wind vane. The buoy orients vane into the wind, such that this beam is, on average, 60 degrees counterclockwise with the mean motion direction, avoiding measurement of the buoy's own wake. Average beam orientations in ice were typically similar to those in open water (i.e., changes in wave direction due to ice do not appear to change the buoy orientation, which would otherwise potentially contaminate the turbulence measurements).

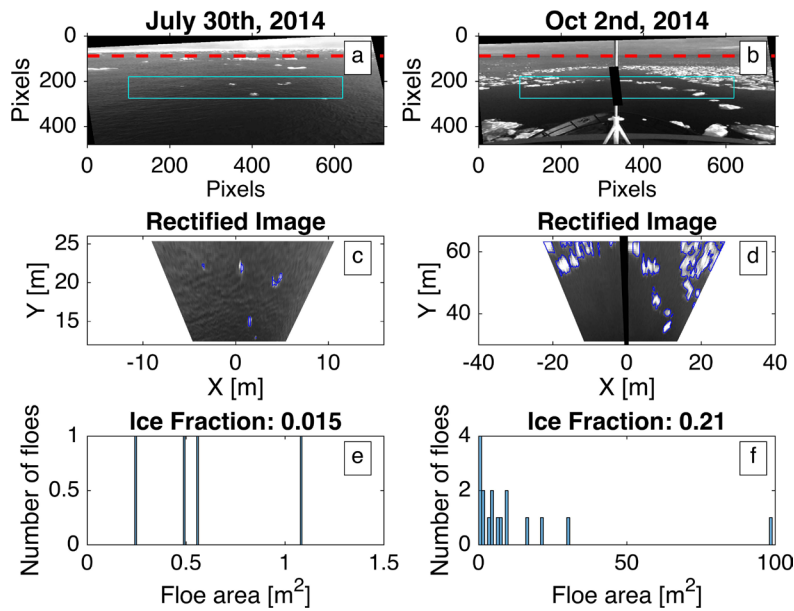


**Figure 2**  
Video processing.

Examples of video processing from the *Ukpik*, July 30th, 2014 (left), and from the *Norseman II*, October 2nd, 2014 (right), deployments are shown above. The stabilized images from the horizon-finding algorithm are shown in (a) and (b), with the identified horizon in red, and the region of interest outlined in teal. An image mask covered a guy-wire centered in the *Norseman II* camera's view frame (b). Panels (c) and (d) show the image rectified to real world coordinates, and filtered with a top hat filter. The blue outlines show the 20% pixel intensity contours. Panels (e) and (f) show histograms of the estimated floe areas, and the fraction of ice coverage in the image.

doi: 10.12952/journal.elementa.000095.f002

### Ice fraction

Ice fractions were estimated from shipboard video observations using a bullet camera (Sony 1/3" ExView B/W CCD) with a horizontal resolution of 600 TVL. On the R/V *Ukpik*, the camera was mounted above the wheelhouse, 4 m above the ocean surface, looking forward of starboard beam. On the R/V *Norseman II*, the camera was mounted at 10.3 m above the ocean surface, looking forward. Data collected at 15 Hz were subsampled to 1 Hz for processing. The camera was stabilized mechanically by a pan and tilt, and images were further stabilized in processing with the horizon method of Schwendeman and Thomson (2015).

Images were rectified to real world coordinates, and filtered with a top hat filter to even illumination and help identify edges. Ice was identified as pixels above the 20% intensity threshold. Ice fraction was estimated as the area of thresholded pixels over the total number of pixels. Floe areas were estimated using MATLAB's *bwlabel* and *bwarea* functions. Example images from the *Ukpik* on July 30th and the *Norseman II* on October 2nd are shown (Figure 2).

Sun glare often caused spuriously high ice fractions, and would result in a large number of small area flows. Therefore, identified areas of less than three pixels were not included in ice estimates. The 1-Hz ship-based ice estimates were matched with the 10-minute SWIFT buoy bursts by taking the mean fraction and floe area observed within 200 m and 5 minutes of the centered buoy location and time. Therefore, the total area used in estimating ice fraction extents beyond the roughly (15 m × 15 m) and (40 m × 40 m) footprints shown in individual frames (Figure 2c and d). However, the total area considered for each ice fraction measurement is small when compared to even high resolution model grid cells (typically between 3 and 30 km). On October 2nd, when no co-located, co-temporal ship-based measurements of ice fraction were available, the fraction was taken in a nearest neighbor interpolation guided qualitatively by the images from a camera onboard the buoy. The buoy's onboard camera did not have a large enough field of view for an accurate, independent, ice fraction measurement, but qualitatively compared well with the nearest ship measurements.

## Results

Wind speeds, wave heights, energy-averaged wave periods, and ice fractions are shown in Figure 3 for the deployments on July 30th, October 2nd, and for the unaccompanied buoy shortly before and after it encountered ice on August 31st. For each deployment, a nearby open water buoy provides context for the relative changes in bulk wave parameters due to ice. In general, the trend is decreased wave heights and increased averaged periods relative to open water values. On July 30th, the open water buoy, a Datawell Waverider, was processed at 3-minute intervals with energy spectra reported in the frequency range ( $0.025 < f < 0.635$  Hz). The difference in frequency bands may explain the discrepancy between the Waverider and SWIFT wave heights in open water. The Waverider was not equipped with an anemometer, thus no secondary wind speed measurement is shown in Figure 3a. The unaccompanied buoys were much farther apart (approximately 20 km) than the buoys on July 30th and October 2nd (approximately 5 km or less); however, the wind and wave measurements were similar when both buoys were in open water, suggesting a valid open water comparison to the in-ice measurements.

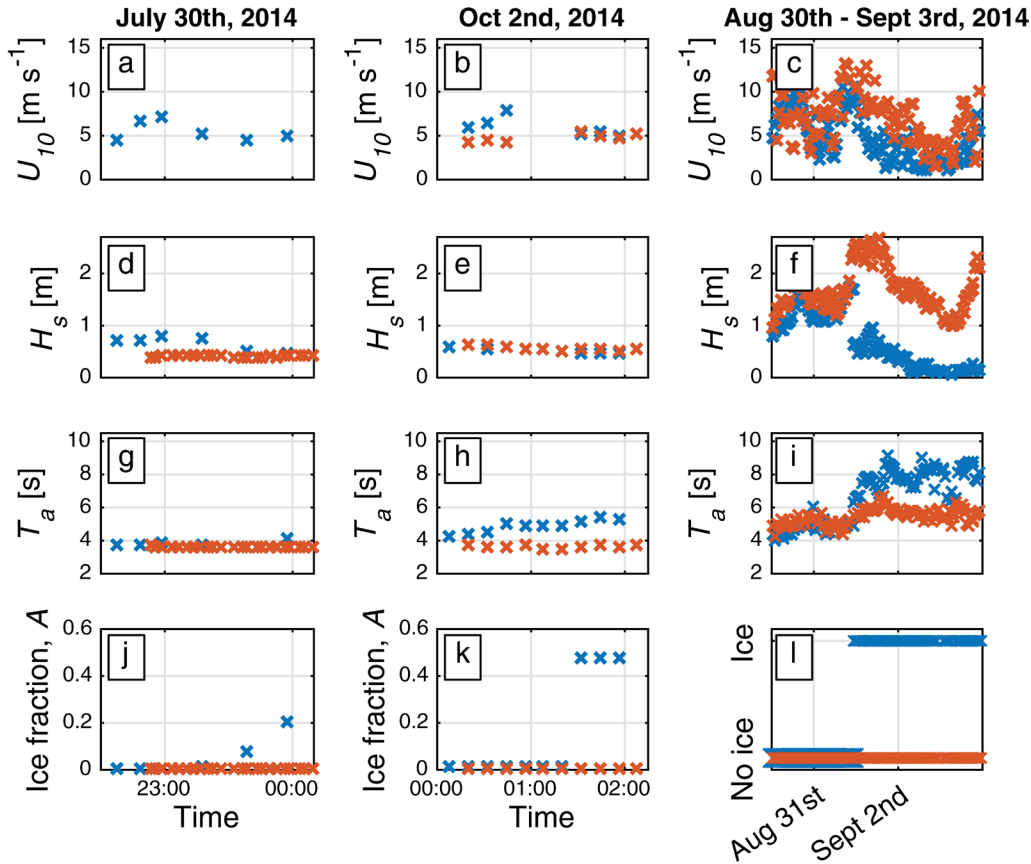


**Figure 3**  
Wind speed, wave height and period, and ice fraction.

Measurements of wind speed ( $U_{10}$ , in a–c), significant wave height ( $H_s$ , in d–f), average wave period ( $T_a$ , in g–i), and ice fraction ( $A$ , in j–l) from the two ship-based deployments and for the unaccompanied buoys are shown. Blue represents buoys that transitioned into ice, while orange represents nearby, open water measurements. Wind speed measurements for open water are not available for the July 30th deployment (a), as the Waverider buoy was not equipped with an anemometer. The onboard camera for the endurance deployment confirmed the presence or absence of ice (I) but did not provide sufficient field of view to estimate ice fraction.

doi: 10.12952/journal.elementa.000095.f003

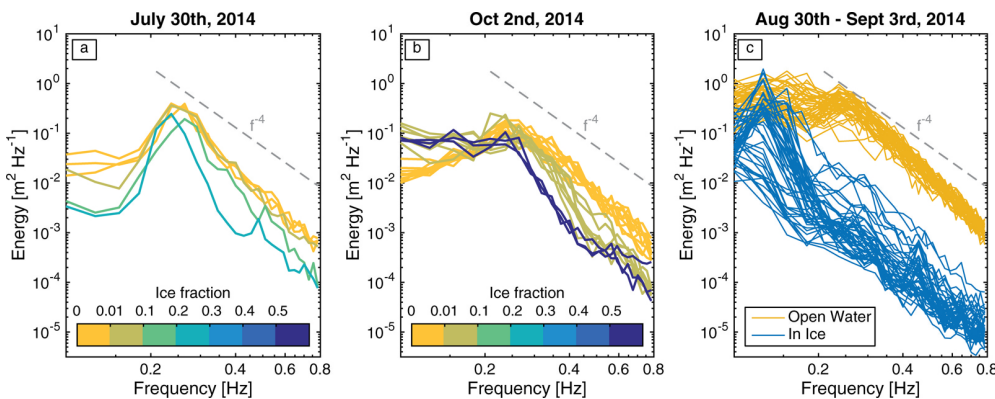
The increases in average period with increased ice fraction, seen in Figure 3, are a result of the reduction of high frequency energy in the wave spectra, shown in Figure 4. Energy at low frequencies (longer periods) were seen to persist in the ice floes, while high frequencies (short waves) had energy levels 10–100 times less than buoys in open water. For the unaccompanied buoy, an onboard camera confirmed the presence of ice during this time, but did not provide sufficient field of view to estimate ice fraction. The observed decreases of high frequency wave energy in ice, reported here, are qualitatively consistent with the previous observations of wave spectra in ice (Wadhams et al., 1986; Doble and Bidlot, 2013; Collins-III et al., 2015).

Spectral wave directions and spread are given in Figure 5, where the difference in wave and wind direction is shown as  $\cos(\theta_r)$ , and the directional spread as,  $\sigma_\theta$ . In open water, wind and wave directions appear to be approximately aligned. Measurements in ice show decreased alignment of wind and waves, especially in the high frequency components. This effect was most apparent in the October 2nd data (Figure 5b), where, in 1% and 50% ice fraction,  $\cos(\theta_r)$  values at frequencies above 0.4 Hz are near zero. In addition, in-ice directional spreads on October 2nd (Figure 5e) are increased above 0.4 Hz. Both the wind/wave misalignment and increased directional spread indicate wave scattering due to ice at the high frequencies, qualitatively consistent with Wadhams et al. (1986). The deployments on July 30th and the unaccompanied buoy on August 31st showed a

**Figure 4**  
Wave spectra.

Wave spectral measurements from (a) July 30th, (b) October 2nd, and (c) the endurance deployment of August 30th–September 3rd, 2014, show energy reduction in ice at high frequencies—as much as 100 times the levels observed in open water with similar wind conditions. Lower frequencies show less attenuation, consistent with previous studies. No shipboard observations of ice fraction (c) are available for the endurance deployment (Figure 3). Gray dashed lines show an  $f^{-4}$  slope for reference.

doi: 10.12952/journal.elementa.000095.f004



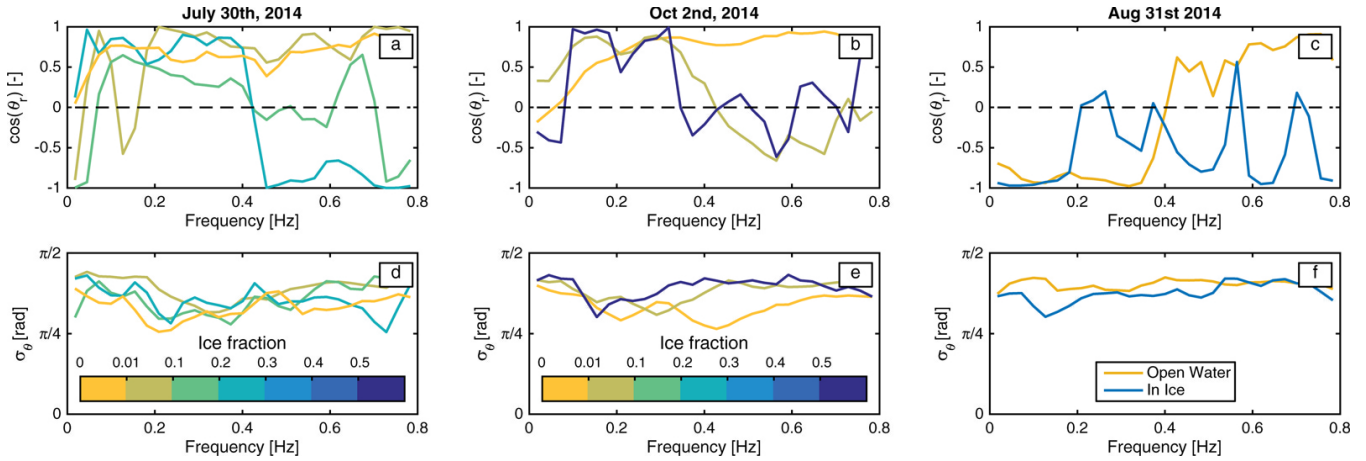


**Figure 5**  
Wave directions and spread.

similar, although less clear, trend, where wind and wave directions do not align in ice at high frequencies. The directional spread of these deployments did not show as clear an effect when compared with the October 2nd data. For the unaccompanied buoy (Figure 5f), the spread appears to decrease slightly in ice, but the open water directional spreads are relatively large compared with the other open water measurements (Figure 5d, and e). This effect is possibly due to a decrease of local wind, from  $U_{10} = 10 \text{ m s}^{-1}$  early on August 31st, to  $U_{10} < 5 \text{ m s}^{-1}$  by September 2nd (Figure 3c).

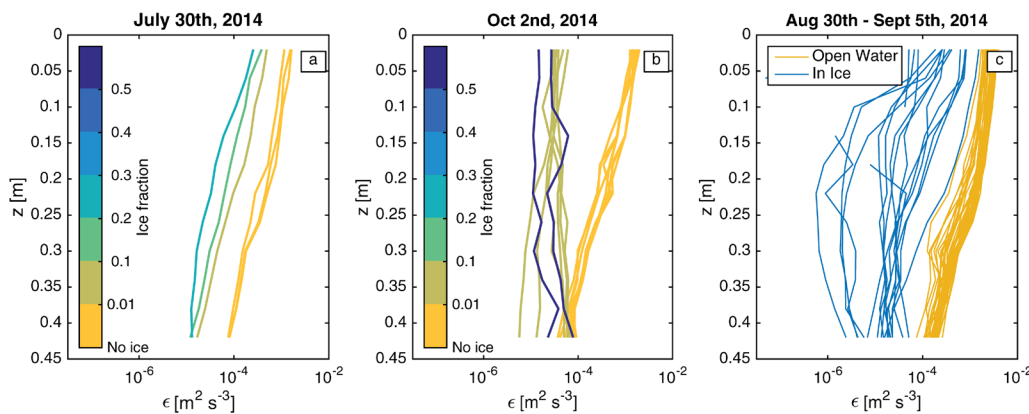
Near-surface TKE dissipation rates from all deployments also showed large reductions in the marginal ice zone (Figure 6). The decreases are one to two orders of magnitude, even for small fractions of ice coverage. This effect was accentuated at the surface in one case ( $z < 0.3 \text{ m}$ ; Figure 6b) when compared to the more uniform reductions in turbulence in another (Figure 6a). We speculate that the more depth-uniform, in-ice profiles on October 2nd may be due to ice-sourced turbulence introduced below the surface, as the buoy was visually observed to drift closer to ice floes during this deployment. Profiles from the unaccompanied buoy deployment (Figure 6c) showed both uniform and non-uniform reductions in TKE dissipation rate. Some profiles were truncated near the surface due to acoustic reflections off of ice floes, which contaminate the data.

Damping, directional scattering, and increased directional spread serve to effectively decrease the wind input term,  $S_{wind}$  a function of both  $E(f)$  and  $\cos(\theta_r)$  (Equation 2). High frequency contributions to  $S_{wind}$  are weighted larger than those at low frequency, both due to the  $\omega$  in Equation 2, and to the  $(1/c)^2$  (here, we use deep water dispersion,  $c = g/\omega$ ) component of the Plant (1982) parameterization for  $\beta$  (Equation 3). Thus, preferential wave damping and scattering at high frequencies can result in a large decrease of the total flux from wind into waves. These large reductions in flux,  $F$  (Equation 4), were seen to be in approximate balance with ocean surface TKE dissipation rates (Figure 7). Some estimates of  $F$  were negative due to contributions from  $\cos(\theta_r)$ , and were not included in Figure 7; the negative values would imply waves doing work on the wind. Error bars for  $F$  represent the uncertainty of the constant in  $\beta$  (Equation 3), and do not include uncertainties in wave spectral or wind stress measurements. Error bars for TKE dissipation rate were estimated from the confidence intervals when fitting the structure function to an  $r^{2/3}$  dependence (Equation 12). The data in Figure 7 correlate in log space across three decades ( $R^2 = 0.66$ , or  $R^2 = 0.86$  without the unaccompanied buoy data of early September, with its reduced fidelity owing to the assumption of a drag coefficient). Most of the data fall close to the 1:1 line, although TKE dissipation rates were larger on average. The correlation was weakest for the lowest dissipation rates where instrument noise is relatively larger, and for the unaccompanied

Wave spectral directions ( $\cos(\theta_r)$ , in a–c) and spread ( $\sigma_\theta$ , in d–f) are shown from July 30th (a and d), October 2nd (b and e), and the unaccompanied buoy when it entered ice ( $\pm 4 \text{ h}$  of the open water/ice transition) on August 31st (c and f). Scattering appears at high frequencies when the buoys drifted into partial ice cover. Directional spread increased for these frequencies on October 2nd, and somewhat on July 30th. For visual clarity, the median relative directions and spreads are shown for each ice fraction bin, rather than each profile (as in Figure 4).

doi: 10.12952/journal.elementa.000095.f005

**Figure 6**  
Dissipation rate profiles of turbulent kinetic energy.



Ocean turbulence profiles in the top 45 cm are shown from (a) July 30th, (b) October 2nd, and (c) the unaccompanied deployment August 30th–September 5th, 2014. The dissipation rate of turbulent kinetic energy,  $\epsilon(z)$ , was reduced up to two orders of magnitude in partial ice cover when compared to similar open water wind conditions.

The reduction of turbulence in the marginal ice zone is consistent with reduced energy in the wave field. No shipboard observations of ice fraction (c) are available for the endurance deployment (Figure 3).

doi: 10.12952/journal.elementa.000095.f006

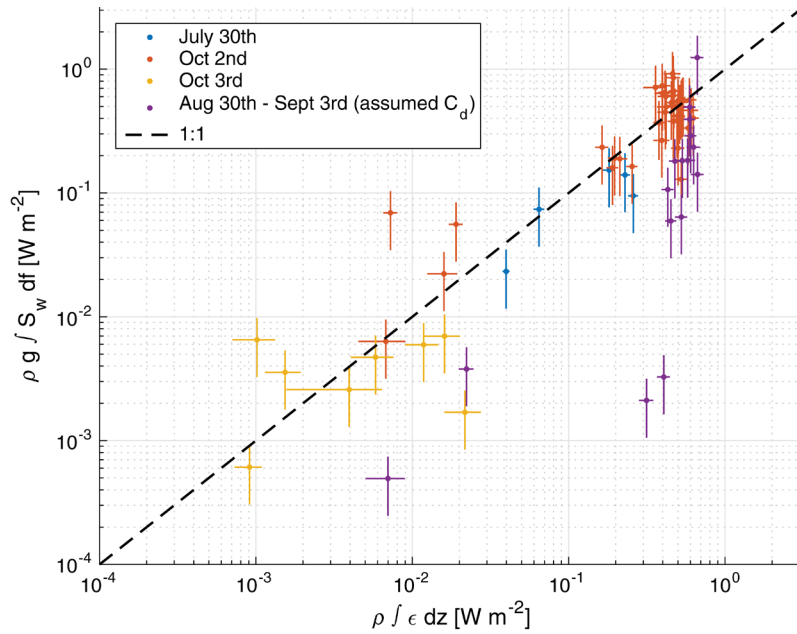


**Figure 7**

**Wind input and ocean turbulence.**

The estimated energy fluxes from wind to waves ( $\rho g \int S_{wind} df$ ), are plotted against the vertically integrated ocean TKE dissipation rates ( $\rho \int \epsilon dz$ ). No wind stress measurements were available for the unaccompanied buoy (purple): therefore,  $u_w$  was estimated using the buoy-measured windspeed and a drag coefficient. Measurements fall approximately on the 1 : 1 line, suggesting that the local wind energy flux to the waves sets the near-surface turbulence rates. Some estimates of  $F$  were negative due to contributions from  $\cos(\theta)$ , and were not included. Error bars for  $F$  represent the uncertainty of the constant in  $\beta$  (Equation 3), and do not include uncertainties in wave spectral or wind stress measurements. Error bars for TKE dissipation rates were estimated from the confidence intervals when fitting the structure function to an  $r^{2/3}$  dependence (Equation 12).

doi: 10.12952/journal.elementa.000095.f007

buoy where a drag coefficient is assumed in the wind source term. These are also the conditions in which ice-ocean shear from mean ice flow and lower frequency wave motions might cause turbulence dissipation not directly related to local wind-wave input

## Discussion

Our measurements indicate that the local input and dissipation of wave energy (shown in Figure 7) are generally not as large as the spatial gradients in wave energy flux,  $\partial(Ec_g)/\partial x$ , which we assume to be from wave-ice interactions,  $S_{ice}$ . A robust form of the ice dissipation term,  $S_{ice}$  is actively being pursued (Liu and Mollo-Christensen, 1988; Liu et al., 1991; Tolman, 2003; Wang and Shen, 2010b; Rogers and Orzech, 2013). The focus of this study was not to attempt to quantify  $S_{ice}$ , but the effects of  $S_{ice}$  are clearly important to the local balance, because  $S_{ice}$  is setting  $\omega E(\omega)$  which in turn sets  $S_{wind}$  for any given wind forcing. We estimated the gradient of wave energy flux between open water and in-ice measurements,  $\partial(Ec_g)/\partial x$ , to be roughly  $1 \text{ W m}^{-2}$  for July 30th, and  $10 \text{ W m}^{-2}$  on October 2nd, and August 31st. These estimates assume  $\partial x$  to be the distance between buoys, rather than along ray paths (i.e., directional information was not used). However, these estimates are as big as, or larger than, the largest measured near-surface dissipation rates or estimated wind inputs, about  $1 \text{ W m}^{-2}$ , in open water. Therefore, we assume that waves first lose energy to  $S_{ice}$ . The ice damping effects (shown in Figure 4) and scattering effects (shown in Figure 5) then reduce the magnitude of the wind input term. Since the damping is stronger at high frequencies, a local balance of wind input and dissipation still occurs. Restated, the waves lose energy to ice, and then, in a feedback, the waves are less effective at gaining energy from a given wind forcing. This effect, in turn, reduces the surface turbulence at a given wind forcing.

We also estimated that directional scattering is more important than wave damping in reducing the flux of energy from wind to waves. Table 1 shows rough estimates of the relative importance of damping and scattering for the three deployments. Scattering was quantified with the ratio of integrated relative

**Table 1. Rough estimates of the relative importance of damping and scattering for the three deployments**

Quantification <sup>a</sup>	July 30th	October 2nd	August 31st
$\frac{\int \cos(\theta)_{ice} df}{\int \cos(\theta)_{open} df}$	0.38	0.19	0.10
$\frac{E_{ice}}{E_{open}}$	0.62	0.73	0.11

<sup>a</sup>Scattering was quantified with the ratio of in-ice to open water integrated relative directions in frequency ( $\cos(\theta)$ ) such that a lower value represents a greater reduction relative to open water. Damping was quantified as the ratio of in-ice to open water wave energy ( $E$ ), proportional to  $H_s^2$ .

doi: 10.12952/journal.elementa.000095.t001

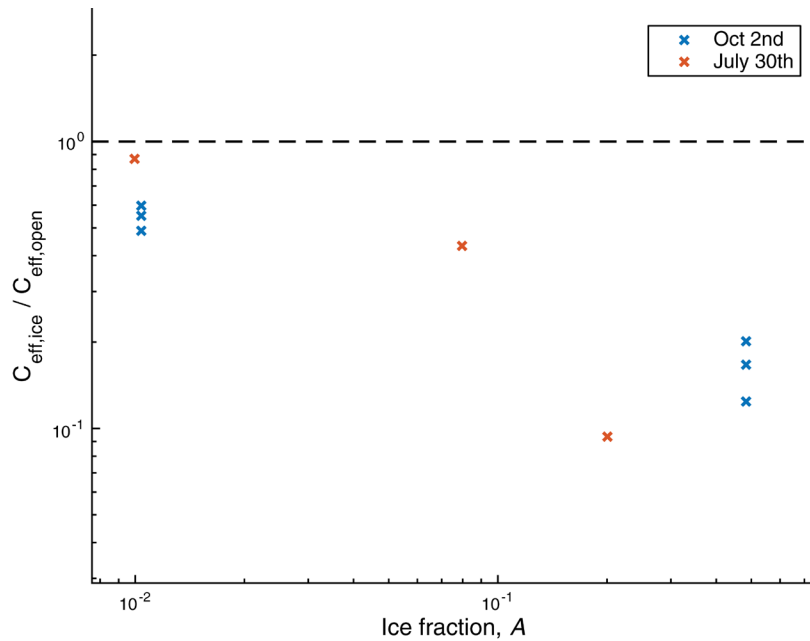


**Figure 8**  
Effective transfer velocity.

The ratio of effective transfer velocity in ice ( $c_{eff,ice}$ ) to nearby open water conditions ( $c_{eff,open}$ ) are plotted against ice fraction. The effective transfer velocity in open water is taken as the mean value of the nearby open water measurements. The in-ice transfer velocities are up to an order of magnitude smaller than the nearby open water counterparts, showing the decrease in energy flux from wind to waves.

doi: 10.12952/journal.elementa.000095.f008

directions in frequency,  $\int \cos(\theta) d\theta$ , such that a lower value represents a greater reduction relative to open water. Damping was quantified as the ratio of in-ice to open water wave energy, proportional to  $H_i^2$ . For July 30th and October 2nd, the scattering ratio was less than the wave energy ratio, while on August 31st, the ratios were approximately equal. The difference in the scattering ratio between deployments was likely an effect of the relative misalignment of wind and waves, and large directional spread before the unaccompanied buoy entered ice (Figure 5c and f), and the larger fraction of energy lost relative to open water (Figure 4), when compared with the deployments on July 30th and October 2nd.

### *The effective transfer velocity, $c_{eff}$*

The effective transfer velocity,  $c_{eff}$  was estimated from the flux,  $F$ , (Equation 4), and the wind stress,  $\tau$ , as  $c_{eff} = F/\tau$ . Figure 8 shows the ratio of in-ice to open water transfer velocity,  $c_{eff,ice}/c_{eff,open}$  with respect to ice fraction. Here, open water values were averaged when estimating,  $c_{eff,open}$ . We observed effective transfer velocities an order of magnitude lower relative to nearby open water estimates; in effect a less efficient transfer of mechanical energy from atmosphere. The largest reductions in  $F$  were seen on October 3rd, and in early September (Figure 7), but the respective transfer velocities are not shown in Figure 8 due to the unspecified ice fraction. Since  $c_{eff}$  encapsulates the total wave spectral changes due to ice as they affect  $F$ , the presentation in Figure 8 by ice fraction is overly simplistic, but still may be useful to understand an overall effect of partial cover.

### *Wind source term*

More recent parameterizations for  $\beta$  (e.g., Donelan and Pierson, 1987; Chalikov and Belevich, 1993) have been shown to reduce scatter in measurements of wave growth rates. In this study, we chose the Plant (1982) parameterization for simplicity. We do not expect that the balance shown in Figure 7 would vary drastically if alternate forms of  $\beta$  were used to estimate  $F$ , as wave damping accounts for a significant fraction of the decreases of  $F$  in ice, and  $E(f)$  is independent of  $\beta$  (Equation 4). Furthermore, the directional contributions from  $\cos(\theta)$  are analogous between parameterizations, and likely, wave scattering will result in a similar reduction of wind input. Often, negative  $\cos(\theta)$  components (i.e., energy flux from waves to wind) are not included in wave models (e.g. Tolman and Chalikov, 1996). The scattering of waves in ice, however, results in many negative relative directional components (i.e., Figure 5), and thus wind input in ice may be sensitive to treatment of these negative components.

A commonality in the aforementioned wind input parameterizations is the dependence on wave phase speed,  $c$ . In this study we assumed the deep water dispersion relation, where wave phase speed  $c = g/\omega$ . However field (Liu et al., 1991; Fox et al., 2001), laboratory (Wang and Shen, 2010a), and theoretical (Untersteiner, 1986; Wang and Shen, 2010b) studies have shown that the dispersion relation of waves in ice differs from

open water values, and would therefore be expected to modify the phase speed,  $c(\omega)$ . For example, the results of Liu et al. (1991) suggest faster wave phase speeds in ice for wave periods less than 14 seconds, and slower phase speeds for wave periods above 14 seconds. These effects would increase the wind input from the low frequencies that were seen to persist farther into the ice pack, and decrease wind input for short, developing waves, when compared to open water.

### *Mechanisms for wave dissipation*

Visual observations, shipboard video, and onboard buoy cameras showed little to no wave breaking in partial ice cover. This finding is consistent with the damping of short, steep waves which would otherwise be expected to break in similar open water environments. We have shown a quasi-equilibrium between the local wind input and the turbulent dissipation, and implicitly assumed that the near-surface turbulent dissipation rates were sourced from wave dissipation: however, wave dissipation is often attributed to wave breaking. The lack of visible wave breaking calls into question the source of near-surface turbulence. The study of Sutherland and Melville (2015) has recently shown that dissipation by micro-breaking (breaking without forming a whitecap) also scales with wind input. This micro-breaking was only visible in infrared, and therefore would provide a pathway for wave dissipation consistent with the lack of observed whitecapping in partial ice cover. In the absence of (or in addition to) micro-breaking, viscous attenuation of waves by ice, and wave-induced shear, could also generate surface turbulence. In this scenario, the ice source/sink,  $S_{ice}$ , would replace the wave-breaking sink,  $S_{diss}$ , that commonly balances  $S_{wind}$  in the radiative transfer equation.

### *Implications for drag coefficients*

Sea ice complicates the exchange of momentum at the ocean surface by balancing a portion of the wind stress. Steele et al. (1989) partitioned the wind stress,  $\tau_{air}$ , linearly by ice fraction,  $A$ ,

$$\tau_{air} = \rho u_*^2 = \rho[(1 - A)C_{d,ocean} + AC_{d,ice}]U_{10}^2. \quad (13)$$

In the open ocean, the drag coefficient,  $C_{d,ocean}$  is a function of wind speed, wave parameters, and fetch or time limitations (Hwang, 2005), and  $C_{d,ice}$  has been shown to depend on ice fraction, floe geometry, melt ponds, ridges, and floe separation distance (Tsamados et al., 2014). Measurement of the individual drag coefficients is especially challenging in partial ice cover, because  $C_{d,ocean}$  and  $C_{d,ice}$  are not uniquely specified by  $U_{10}$  and  $u_*$  (Equation 13). However, it is not clear that use of the open water ocean drag coefficients is valid in partial ice cover, as wave-ice interactions alter wave spectra through damping and scattering. This study does not have a sufficient number of measurements across a range of  $A$ ,  $U_{10}$  to fully parameterize  $C_{d,ocean}$ . Instead, we estimated average ice and ocean drag coefficients using all available data with  $A > 0$  in a least squares sense by solving the matrix equation,

$$\begin{bmatrix} u_{*1}^2 \\ \vdots \\ u_{*n}^2 \end{bmatrix} = \begin{bmatrix} (1 - A_1)U_{10,1}^2 & A_1U_{10,1}^2 \\ \vdots & \vdots \\ (1 - A_n)U_{10,n}^2 & A_nU_{10,n}^2 \end{bmatrix} \begin{bmatrix} C_{d,ocean} \\ C_{d,ice} \end{bmatrix}. \quad (14)$$

Here, the subscripts 1 ...  $n$  represent separate measurements. We found  $C_{d,ocean} = 1.0 \times 10^{-3}$  and  $C_{d,ice} = 2.8 \times 10^{-3}$ , using MATLAB's *mldivide* function. These estimates are comparable to open water drag coefficients at low wind speeds (see Hwang, 2005), and drag for brash ice and rough marginal ice zone floes (Guest and Davidson, 1991). The data used to estimate drag coefficients (shown in Figure 3), had wind speeds of  $U_{10} < 10 \text{ m s}^{-1}$ ,  $H_s < 1 \text{ m}$ ,  $T_s < 6 \text{ s}$ , and ice fractions ranging from 1 to 50%.

## Summary

The use of measured winds, waves, turbulence, and ice from the marginal ice zone has indicated that wave energy at high frequencies is strongly damped into the ice pack, while energy at low frequencies persists, consistent with previous studies. Spectral estimates of wave direction and spread indicate scattering primarily in the high frequencies. Turbulent dissipation rates within 0.5 m of the free surface were reduced up to two orders of magnitude in partial ice cover when compared to nearby open water measurements. When depth-integrated, the ocean TKE dissipations roughly matched estimates of energy flux from the frequency-integrated wind source term across nearly three orders of magnitude. In partial ice cover, wind input occurred primarily at the low frequencies of the wave spectrum which did not experience significant damping or scatter. In contrast, the mechanism for wave dissipation, its frequency dependence, and subsequent turbulence generation is less clear. The local balance of wind input and surface turbulence is seen to be dependent on the ice-modified wave field, in addition to the wind stress. Thus, prediction of ocean surface turbulence in the

marginal ice zone would necessitate knowledge of open water wave parameters and ice attenuation. Finally, an average air-ocean drag coefficient of  $C_{d,ocean} = 1.0 \times 10^{-3}$  has been estimated from ice fractions of 1–50% and wind speeds less than  $10 \text{ ms}^{-1}$ .

## References

- Agrawal Y, Terray EA, Donelan MA, Hwang PA, Williams III AJ, et al. 1992. Enhanced dissipation of kinetic energy beneath surface waves. *Nature* 3(59): 219–220. doi: 10.1038/359219a0.
- Chalikov DV, Belevich MY. 1993. One-dimensional theory of the wave boundary layer. *Bound-Lay Meteor* 63: 65–96.
- Collins-III CO, Rogers WE, Marchenko A, Babanin AV. 2015. In situ measurements of an energetic wave event in the Arctic marginal ice zone. *Geophys Res Lett* 42. doi: 10.1002/2015GL063063.
- Comiso JC, Nishio F. 2008. Trends in the sea ice cover using enhanced and compatible AMSR-E, SSM/I, and SMMR data. *J Geophys Res* 113(C02S07). doi: 10.1029/2007JC004257.
- Comiso JC, Parkinson CL, Gersten R, Stock L. 2008. Accelerated decline in the Arctic sea ice cover. *Geophys Res Lett* 35(L01703). doi: 10.1029/2007GL031972.
- Craig PD, Banner ML. 1994. Modeling wave-enhanced turbulence in the ocean surface layer. *J Phys Oceanogr* 24: 2546–2559.
- D'Asaro EA, Thomson J, Shcherbina AY, Harcourt RR, Cronin MF, et al. 2014. Quantifying upper ocean turbulence driven by surface waves. *Geophys Res Lett* 41: 1–6. ISSN 1944-8007. doi: 10.1002/2013GL058193.
- Doble MJ, Bidlot JR. 2013. Wave buoy measurements at the Antarctic sea ice edge compared with an enhanced ECMWF WAM: Progress towards global waves-in-ice modelling. *Ocean Modelling* 70: 166–173.
- Donelan MA, Pierson WJ. 1987. Radar scattering and equilibrium ranges in wind-generated waves with application to scatterometry. *J Geophys Res* 92(C5): 2971–5029. doi: 10.1029/JC092iC05p04971.
- Fox C, Haskell TG, Chung H. 2001. Dynamic, in-situ measurement of sea-ice characteristic length. *Ann Glaciol* 33: 339–344.
- Francis OP, Panteleev GG, Atkinson DE. 2011. Ocean wave conditions in the Chukchi Sea from satellite and in situ observations. *Geophys Res Lett* 38(L24610). doi: 10.1029/2011GL049839.
- Gemmrich J, Mudge T, Polonichko V. 1994. On the energy input from wind to surface waves. *J Phys Oceanogr* 24: 2413–2417.
- Goring DG, Nikora VI. 2002. Despiking acoustic doppler velocimeter data. *J Hydraul Eng* 128(1): 117–126.
- Guest PS, Davidson KL. 1991. The aerodynamic roughness of different types of sea ice. *J Geophys Res* 96(C3): 4709–4721.
- Herbers THC, Jessen PF, Janssen TT, Colbert DB, MacMahan JH. 2012. Observing ocean surface waves with GPS-tracked buoys. *J Atmos Ocean Tech* 29: 944–959.
- Hwang PA. 2005. Temporal and spatial variation of the drag coefficient of a developing sea under steady wind-forcing. *J Geophys Res Oceans* 110(C07024). doi: 10.1029/2005JC002912.
- Kohout AL, Williams MJM, Dean SM, Meylan MH. 2014. Storm-induced sea-ice breakup and the implications for ice extent. *Nature* 509: 604–607. doi: 10.1038/nature13262.
- Lamont JC, Scott DS. 1970. An eddy cell model of mass transfer into the surface of a turbulent liquid. *Am Inst Chem Eng* 16: 512–519.
- Large W, Pond S. 1981. Open ocean momentum flux measurements in moderate to strong winds. *J Phys Oceanogr* 11: 324–336.
- Liu AK, Holt B, Vachon PW. 1991. Wave propagation in the Marginal Ice Zone: Model predictions and comparisons with buoy and Synthetic Aperture Radar data. *J Geophys Res* 96(C3): 4605–4621.
- Liu AK, Mollo-Christensen E. 1988. Wave propagation in a solid ice pack. *J Phys Oceanogr* 18: 1702–1712.
- Loose B, McGillis WR, Perovich D, Zappa CJ, Schlosser P. 2014. A parameter model of gas exchange for the seasonal ice zone. *Ocean Sci* 10: 17–28.
- Martin T, Steele M, Zhang J. 2014. Seasonality and long-term trend of Arctic Ocean surface stress in a model. *J Geophys Res Oceans* 119(1723–1738). doi: 10.1002/2013JC009425.
- Mori N, Suzuki T, Kakuno S. 2007. Noise of acoustic Doppler velocimeter data in bubbly flow. *ASCE J Eng Mechanics* 133(1): 122–125. doi: 10.1061/(ASCE)0733-9399(2007)133:1(122).
- Phillips OM. 1985. Spectral and statistical properties of the equilibrium range in wind-generated gravity waves. *J Fluid Mech* 156: 495–531.
- Plant B. 1982. A relationship between wind stress and wave slope. *J Geophys Res* 87: 1961–1967.
- Rainville L, Lee CM, Woodgate RA. 2011. Impact of wind-driven mixing in the Arctic Ocean. *Oceanography* 24(3): 136–145.
- Rogers WE, Orzech MD. 2013. Implementation and testing of ice and mud source functions in WAVEWATCH III, NRL Memorandum Report. NRL/MR/7320-13-9462, 31 pp.
- Schwendeman M, Thomson J. 2015. A horizon-tracking method for shipboard video stabilization and rectification. *J Atmos Ocean Tech* 32: 164–176.
- Squire VA. 2007. Of ocean waves and sea ice revisited. *Cold Regions Sci Tech* 49: 110–133.
- Steele M, Morison JH, Untersteiner N. 1989. The partition of air-ice-ocean momentum exchange as a function of ice concentration, floe size, and draft. *J Geophys Res* 94: 12739–12750.
- Sutherland P, Melville WK. 2015. Field measurements of surface and near-surface turbulence in the presence of breaking waves. *J Phys Oceanogr* 45: 943–965.
- Terray E, Donelan M, Agrawal Y, Drennan W, Kahma K, et al. 1996. Estimates of kinetic energy dissipation under breaking waves. *J Phys Oceanogr* 26: 792–807.
- Thomson J. 2012. Wave breaking dissipation observed with SWIFT drifters. *J Atmos Ocean Tech* 29(12): 1866–1882. doi: 10.1175/JTECH-D-12-00018.1.
- Thomson J, Rogers WE. 2014. Swell and sea in the emerging Arctic Ocean. *Geophys Res Lett* 41. doi: 10.1002/2014GL059983.
- Thorpe SA. 2004. Langmuir circulation. *Annu Rev Fluid Mech* 36: 55–79. doi: 10.1146/annurev.fluid.36.052203.071431.
- Tolman HL. 2003. Treatment of unresolved islands and ice in wind wave models. *Ocean Modeling* 5: 219–231.
- Tolman HL, Chalikov D. 1996. Source terms in a third-generation wind wave model. *J Phys Oceanogr* 26: 2497–2518.

- Tsamados M, Feltham DL, Schroeder D, Flocco D, Farrell SL, et al. 2014. Impact of variable atmospheric and oceanic form drag on simulations of Arctic Sea Ice. *J Phys Oceanogr* **44**: 1329–1353.
- Untersteiner N, ed. 1986. *The Geophysics of Sea Ice*. New York: Plenum.
- Wadhams P, Squire VA, Ewing JA, Pascal RW. 1986. Effect of the marginal ice zone on the directional wave spectrum of the ocean. *J Phys Oceanogr* **16**: 358–376.
- Wadhams P, Squire VA, Goodman DJ, Cowan AM, Moore SC. 1988. The attenuation rates of ocean waves in the marginal ice zone. *J Geophys Res* **93**(C6): 6799–6818.
- Wang R, Shen HH. 2010a. Experimental study on surface wave propagating through a grease-pancake ice mixture. *Cold Regions Sci Tech* **61**: 90–96. doi: 10.1016/j.coldregions.2010.01.011.
- Wang R, Shen HH. 2010b. Gravity waves propagating into an ice-covered ocean: A viscoelastic model. *J Geophys Res* **115**(C06024). doi: 10.1029/2009JC005591.
- Wang XL, Feng Y, Swail VR. 2015. Historical changes in the Beaufort-Chukchi-Bering Seas surface winds and waves, 1971–2013. *J Climate* **28**: 7457–7469. doi: 10.1175/JCLI-D-15-0190.1.
- Wiles P, Rippeth TP, Simpson J, Hendricks P. 2006. A novel technique for measuring the rate of turbulent dissipation in the marine environment. *Geophys Res Lett* **33**: L21608.
- Yelland M, Taylor P, Consterdine I, Smith M. 1994. The use of the inertial dissipation technique for shipboard wind stress determination. *J Atmos Ocean Tech* **11**: 1093–1108.
- Zappa CJ, Raymond PA, Terray EA, McGillis WR. 2003. Variation in surface turbulence and the gas transfer velocity over a tidal cycle in a macro-tidal estuary. *Estuaries* **26**(6): 1401–1415.

#### Contributions

- Contributed to conception and design: SZ, JT
- Contributed to acquisition of data: SZ, JT
- Contributed to analysis and interpretation of data: SZ, JT
- Drafted and/or revised the article: SZ, JT

#### Acknowledgments

Thanks to the field crew, J. Talbert and A. de Klerk. The collection, processing, and curation of the shown SAR imagery was made possible by the National Ice Center, L. Rainville, and H. Graber. Thanks to W. E. Rogers, T. Martin, and two anonymous reviewers for insightful comments. Thanks to M. Steele and J. Morison for helpful conversations and comments.

#### Funding information

Funding was provided by Office of Naval Research as part of the Marginal Ice Zone, Departmental Research Initiative.

#### Competing interests

The authors have no competing interests to declare.

#### Data accessibility statement

SWIFT data are available at <http://www.apl.uw.edu/swift>.

#### Copyright

© 2016 Zippel and Thomson. This is an open-access article distributed under the terms of the Creative Commons Attribution License, which permits unrestricted use, distribution, and reproduction in any medium, provided the original author and source are credited.